Earth System
Dynamics
Discussions

On the interconnections among major climate modes and their common driving factors

Xinnong Pan[1], Geli Wang[1*], Peicai Yang[1], Jun Wang[2], Anastasios A. Tsonis[3,4]

[1] Key Laboratory of Middle Atmosphere and Global Environment Observation (LAGEO), Institute of Atmospheric Physics, Chinese Academy of Sciences, Beijing 100029, China

[2] Key Laboratory of Regional Climate-Environment for Temperate East Asia (RCE-TEA), Institute of Atmospheric Physics, Chinese Academy of Sciences, Beijing 100029, China

[3] Department of Mathematical Sciences, Atmospheric Sciences Group, University of Wisconsin-Milwaukee, Milwaukee 53201, USA

[4] Hydrologic Research Center, San Diego 92127, USA

Correspondence to: Geli Wang (wgl@mail.iap.ac.cn)

22   **Abstract**

23   The variations in oceanic and atmospheric modes on various timescales play important roles in generating

24   regional and global climate variability. Many efforts have been devoted to identify the relationships between

25   the variations in climate modes and regional climate variability, but rarely explored the interconnections

26   among these climate modes. Here we use climate indices to represent the variations in major climate modes

27   and we examine the harmonic relationship among the driving forces of climate modes by the combination of

28   Slow Feature Analysis (SFA) and wavelet analysis. We find that all of the significant peak-periods of

29   driving-force signals in the climate indices can be represented as the harmonics of four base periods: 2.32 yr,

30   3.90 yr, 6.55 yr and 11.02 yr. We infer that the period of 2.32 yr is associated with the signal of Quasi

31   Biennial Oscillation (QBO). The periods of 3.90 yr and 6.55 yr are connected with the intrinsic variability of

32   El Niño-Southern Oscillation (ENSO), and the period of 11.02 yr arises from the sunspot cycle. Results

33   suggest that the base periods and their harmonic oscillations linked to QBO, ENSO and solar activities act as

34   the key connections among the climatic modes with synchronous behaviors, highlighting the important roles

35   of these three oscillations in the variability of current climate.

36   **Key words:** climate modes; slow feature analysis; wavelet analysis; driving forces

37   **Highlights:**

38   i) The harmonic relationship among the driving forces of climate modes was investigated by using Slow

39   Feature Analysis and wavelet analysis.

40   ii) All of the significant peak-periods of driving-force signals in climate indices can be represented as the

41   harmonics of four base periods.

42   iii) The four base periods related to QBO, ENSO and solar activities act as the key linkages among different

43   climatic modes with synchronous behaviors.

1 Introduction

44

45 The influences of large-scale climate modes (e.g., El Niño-Southern Oscillation (ENSO), Pacific Decadal

46 Oscillation (PDO), North Atlantic Oscillation (NAO) and the Atlantic Multi-decadal Oscillation (AMO)) on

47 the variations of regional-to-global climate (e.g. temperature, rainfall, and atmospheric circulations) have

48 been extensively examined (Bradley et al., 1987; Wu et al., 2003; McCabe et al., 2004; Kenyon and Hegerl,

49 2008; Steinman et al., 2015; Wang et al., 2016; 2017; Yang et al., 2017; Zhang et al., 2017; Xie et al., 2019).

50 It has been well established that regional climate variations at various temporal and spatial scales are

51 modulated by the variabilities of major climate modes. For instance, Wu et al. (2003) estimated that about

52 25% rainfall variances in fall and winter over southern China can be explained by ENSO. McCabe et al.

53 (2004) reported that the PDO and AMO have contributed to more than half (52%) of the tempo-spatial

54 variance in multi-decadal drought occurrence over the conterminous Untied States. Xie et al. (2019) found

55 that the multi-decadal variability in East Asian surface air temperature (EASAT) is highly associated with

56 the NAO, which leads detrended annual EASAT by 15-20 years. Based on this relationship, they proposed a

57 NAO-based linear model to predict the near-future change in EASAT.

58

59 The variations of oceanic and atmospheric modes affect regional climate mainly through the teleconnections

60 within the atmosphere (i.e., atmospheric bridge) and ocean (i.e., oceanic tunnel) (Liu and Alexander, 2007).

61 Atmospheric teleconnections can be produced by both external forcings from ocean or land (e.g., sea surface

62 temperature (SST) anomalies related to ENSO) and internal atmospheric processes (e.g. Rossby wave in the

63 westerlies) (Trenberth et al., 1998). Though many theories have been developed to explain the physical

64 mechanisms behind the influences of major climate modes on regional climate, the interconnections among

65 these climate modes *per se*, and their primary driving factors remain largely unclear. Given that remote

66   teleconnections exist between climate modes and regional climate at various temporal and spatial scales,

67   tight interconnections are expected to exist among these climate modes (Rossi et al., 2011). In addition,

68   acted as the main energy source of the climate system, the external forcings of climate system (e.g., solar

69   activities) impose extensive influences on various climate modes (e.g., ENSO and NAO) (Kirov et al., 2002;

70   Velasco et al., 2008). Thus, it appears to be promising to identify the interconnections among major climate

71   modes and their common driving factors.

72

73   As the indicators of climate modes, many climate indices (e.g., the Niño3.4 SST for ENSO) have been

74   proposed and widely used to investigate the dynamic processes and physical mechanisms within climate

75   system (Dai, 2006; Steinman et al., 2015; Wang et al., 2017). However, the major barrier to clarify the

76   interconnections of these climate indices is how to effectively extract the driving forces, and identify their

77   corresponding essential driving factors. It is well recognized that most of the time series observed in the real

78   world are non-stationary because of the effects of external perturbations (Verdes et al., 2001). As a

79   representative non-stationary dynamic system, the driving forces for the variations of major climate modes

80   remain difficult to be determined. Some pioneering works have been conducted to solve this daunting

81   challenge. For example, Yang (2003) proposed a physical conceptual frame that the non-stationary features

82   of climate system are relevant to the characteristics of hierarchical structure: the driving force originating

83   from higher hierarchy sub-system controls the behaviors of lower hierarchy sub-system in a cascade way.

84   Compared to the dynamic reality as manifested in lower hierarchy sub-system, the driving force of higher

85   hierarchy sub-system tends to be a much slower process. In other words, the essential differences between

86   higher and lower sub-systems reflect in scale and energy.

87

88   Many efforts have been devoted to extract the information of driving force from dynamic system (Yang et

89   al., 2016). Slow feature analysis (SFA) is an algorithm that was developed to extract the slowly varying

90   features from non-stationary time series, which provides a direct and effective approach to identify the

91   driving forces of non-stationary dynamic system. Based on idealized models, recent studies have suggested

92   that the SFA can extract slowly-varying driving forces and sub-component signal from fast-varying

93   non-stationary time series even without any prerequisite knowledge about the underlying dynamic system

94   and its driving forces (Wiskott et al., 2002, 2003; Konen et al., 2009, 2011; Escalante-B et al., 2012).

95   Considering that the driving-force signal of dynamic system often consists of different components with

96   various time scales, Pan et al. (2017) detected the independent driving-force factors that contain significant

97   peak-periods from the SFA-extracted signals robustly through combing the SFA with wavelet analysis

98   (Torrence et al., 1998). Recently, this kind of technique that combines the SFA with wavelet analysis also

99   has been successfully applied to detect the external and internal driving-forces signals responsible for the

100   variations of regional climate, such as the drought variability in the southwestern United States (Zhang et al.,

101   2017), the temperature variations in the Central England (Wang et al., 2017) and the Northern Hemisphere

102   (Yang et al., 2016), and the oscillations of stratospheric ozone concentration (Wang et al., 2016). Thus, it is

103   reasonable to anticipate that this new approach can serve for the study of the interconnections among major

104   climate modes and their primary driving factors.

105

106   To this end, we aim to extract the driving forces of major climate modes and identify their interconnections

107   and primary driving factors by the combination of SFA and wavelet analysis. The remainder of this paper is

108   organized as follows. The data and methods used in this study are described in Sections 2 and 3, respectively.

109   The main results are presented in Section 4, followed by the conclusions and discussions in Section 5.

Earth System
Dynamics
Discussions

2 Data

In this study, we choose monthly mean indices for four widely-investigated climate modes (ENSO, PDO, AMO and NAO), which can be easily accessed from NOAA website (www…). Below, we will describe these four climate modes and their corresponding indices briefly.

2.1 ENSO

ENSO is well recognized as a natural ocean-atmosphere coupled mode in the tropical Pacific (Deser et al., 2010), which shows global impacts (Newman et al., 2003). El Niño (La Niña) refers to warming (cooling) phase of the tropical Pacific Ocean occurring every 2-7 yr. Meanwhile, the anomalous warming or cooling conditions are linked to a large-scale east-west seesaw air pressure pattern, referred to Southern Oscillation (Capotondi et al., 2015). El Niño and Southern Oscillation are two manifestations of ENSO phenomenon (Bjerknes, 1969). In this study, ENSO is represented by both Niño 3.4 SST anomalies and Southern Oscillation Indices (SOI). Niño 3.4 index (1870/01-2018/12, hereafter referred to as NINO) is defined as the SST anomalies in the Nino 3.4 region (5ºN-5ºS; 170-120ºW) based on the HadISST1 dataset (Rayner et al., 2003). SOI index (1866/01-2017/12) is calculated from the standardized sea level pressure (SLP) differences measured between the islands of Tahiti and Darwin, Australia (Ropelewski et al., 1987).

2.2 PDO

PDO is the dominant pattern of decadal variability of North Pacific SST, which has been widely-studied in various subjects (Newman et al., 2016). Previous study shows that the changing phase of PDO affects the anomalies of atmospheric circulation around North Pacific Ocean basin, and even the South Hemisphere (Mantua and Hare, 2002). The characteristic period of PDO is 50-60 yr and a warm or cold phase of PDO

132   can typically persist for about 20-30 yr. If PDO is in its positive phase, the North Pacific Ocean turns colder

133   and Middle East Pacific Ocean turns warmer, otherwise it is in negative phase. In this study, PDO is defined

134   by the leading principal component of monthly SST anomalies in the Pacific basin, poleward of 20ºN during

135   1900-2017 (Mantua et al., 1997).

136

137   **2.3 AMO**

138   AMO is a dominant signal of climate variability in the field of North Atlantic SST, which has a statistically

139   significant spectral peak in the 50-70 yr band (Schlesinger et al., 1994; Sun et al., 2015). Related studies

140   suggested that AMO is an inner variability of climate system, which can affect regional-to-hemispheric

141   climate (Zhang, 2007; Knight et al., 2006). The slow variation of the Atlantic meridional overturning

142   circulation (AMOC) is found to play a dominant role in the Atlantic multidecadal variability of SST (Zhang,

143   2017; Delworth et al., 2000; Garuba et al., 2018). In this study, AMO is defined as the detrended

144   area-weighted average SST over the North Atlantic from 0° to 70°N during 1856-2018 based on the Kaplan

145   SST dataset (Enfield et al., 2001). Two versions of AMO indices are available: unsmoothed one and

146   smoothed one. The high-frequency variability of the latter one has been removed out by a 121-month

147   smoother. We choose to use the unsmoothed AMO index in this study.

148

149   **2.4 NAO**

150   The NAO is active in the North Atlantic region that is characterized by a large-scale seesaw in atmospheric

151   mass between the subtropical high and the polar low (Li et al., 2003). It manifests as climate fluctuations at

152   multiple timescales ranging from inter-annual to multi-decadal variabilities (Jones et al., 1997; Li et al.,

153   2013), affecting the climate in and around North Atlantic Ocean basin, and even the entire Northern

154   Hemisphere (Wallace and Gutzler, 1981; Hurrell，1995; Li et al., 2013; Delworth et al., 2016; Jajcay et al.,

155   2016;). Although NAO is most pronounced during the winter, it is the dominant mode of atmospheric

156   circulation in the North Atlantic sector throughout the whole year. Previous study suggested that NAO

157   drives the North Atlantic SST anomalies at the timescale less than 10 yr (Delworth et al., 2017).

158

159   NAO index is typically defined as a meridional dipole mode (which has been lately suggested of being a

160   three-pole pattern (Tsonis et al., 2008)) in atmospheric pressure with two centers of action in Iceland and

161   Azores during 1825-2017. For comparison, we also examine another observationally-based monthly NAO

162   index for the period of 1850-2015 (hereafter referred to as NAOI), which is defined as the difference in the

163   normalized sea level pressure (SLP) that is zonally-averaged over the North Atlantic sector from $80^{o}W$ to

164    $30^{o}E$ between $35^{o}N$ and $65^{o}N$ (Li et al., 2003). NOAI is derived from the HadSLP dataset with the base

165   period of 1961-1990.

166

167   All the climate indices data mentioned above can be downloaded from the NOAA website of climate index

168   time series (www.esrl.noaa.gov/psd/gcos_wgsp/Timeseries/), except that NAOI is obtained from Prof.

169   Jianping Li's homepage in Beijing Normal University (http://ljp.gcess.cn/dct/page/65610). **Fig. 1** shows the

170   normalized native monthly time series of these climate indices.

171

172   **3 Methods**

173   **3.1 Slow Feature Analysis (SFA)**

174   Based on time-embedding theorems, one-dimensional time series can turn into a multidimensional system.

175   For this multidimensional input system, the SFA acts as a nonlinear method that uses a nonlinear expansion

176   to map the input signal into a feature space and solves a linear problem (Blaschke et al., 2006). The

177   objective of SFA is to find instantaneous scalar input-output functions that generate output signals that vary

178   as slowly as possible but still carry significant information. To ensure this, we require the output signals to

179   be uncorrelated and have unit variance (Franzius et al., 2011).

180

181   Consider a time series $\{x(t)\}_{t=t_1,\dots,t_n}$, where t stands for time and n indicates the length of the time series.

182   First, we embed $\{x(t)\}$ into an m-dimensional state space:

183
$$\mathbf{X}(t) = \{x_1(t), x_2(t), \dots, x_m(t)\}_{t=t_1,\dots,t_N}$$

184   where $N = n - m + 1$. Then nonlinear expansions (usually second-order polynomials) are used to generate a

185   k-dimensional function state space:

186    $\mathbf{H}(t) = \{x_1(t), \dots, x_m(t), x_1^2(t), \dots, x_1(t)x_m(t), \dots, x_{m-1}^2(t), \dots, x_m^2(t)\}_{t=t_1,\dots,t_N}$,

187   which can also be written as $\mathbf{H}(t) = \{h_1(t), h_2(t), \dots, h_k(t)\}_{t=t_1,\dots,t_N}$, where

188    $k = m + m(m+1)/2$.

189

190   After that, the expanded signal $\mathbf{H}(t)$ is normalized so that it satisfies the constraints of zero mean and unit

191   variance. This process is referred to as whitening or sphering. Thus, we have

192
$$\mathbf{H}'(t) = \{h_1'(t), h_2'(t), \dots, h_k'(t)\}_{t=t_1,\dots,t_N}, \text{ where}$$

193
$$\bar{h}_j' = 0 \ \text{(zero mean)},$$

194
$$h_j' h_j'^{T} = 1 \ \text{(unit variance)},$$

195
$$h_j'(t) = \left[h_j(t) - \bar{h}_j\right]/S, \text{ and } S = \frac{1}{k}\sqrt{\sum_{j=1}^{k}(h_j(t) - \bar{h})^2}.$$

196   Then, by using Schmidz algorithm, $\mathbf{H}'(t)$ is orthogonized into:

197
$$\mathbf{Z}(t) = \{z_1(t), z_2(t), \dots, z_k(t)\}_{t=t_1,\dots,t_N}.$$

198   Thus, each output signal can be expressed as the following linear combination:

199    $$y(t) = a_1 z_1(t) + a_2 z_2(t) + \dots + a_k z_k(t),$$

200    $(a_1, a_2, \dots, a_k)$ is a set of weighting coefficients.

201

202   Note that the output signals are orthogonal and nontrivial:

203    $$z_i(t) \cdot z_j(t) = 0, \; \overline{z_i}(t) = \overline{z_j}(t) = 0, \; z_j(t) \cdot z_j^T(t) = 1,$$

204

205   Subsequently, we perform the 1$^{\text{st}}$ order differencing on $\mathbf{Z}(t)$ to obtain the derivative function space:

206    $$\dot{z}_j(t_i) = z_j(t_{i+1}) - z_j(t_i)$$

207    $$\dot{\mathbf{Z}}(t) = \{\dot{z}_1(t), \dot{z}_2(t), \dots, \dot{z}_k(t)\}_{t=t_1,\dots,t_N}.$$

208

209   Then we calculate the time-derivative $K \times K$ covariance matrix $\mathbf{B} = \dot{\mathbf{Z}}\dot{\mathbf{Z}}^T$, where its eigenvalues are $\lambda_1 \leq$

210    $\lambda_2 \leq \dots \leq \lambda_k$ and the corresponding eigenvectors are $\mathbf{W}_1, \dots, \mathbf{W}_k$. Finally, using $\mathbf{W}_1$, the driving force can

211   be written as:

212    $$y_1(t) = r\mathbf{W}_1 \cdot \mathbf{Z}(t) + c$$

213   where r and c are two arbitrary constants that resulting from quadrature of $y(t)$ and solution of $\mathbf{W}_1$,

214   respectively.

215

216   **3.2 Wavelet analysis**

217   Wavelet analysis is widely used to analyze localized structures and spectral properties of time series.

218   Torrence (1998) provided a useful toolkit to conduct wavelet analysis step by step including statistical

219   significance   testing.   The   toolkit   can   be   accessed   from   the   website:

220   http://paos.colorado.edu/research/wavelets/.

221

222   Here, we choose to use the Morlet wavelet, which offers a high spectrum resolution. The wavenumber is set

223   to 4, representing a lower resolution wavelet scale to analyze the time-averaged global power spectrum of

224   climate indices. Previous study based on idealized models shows that the significant peak-periods of the

225   SFA-derived signal correspond well to the driving force factors (Pan et al., 2017). Thus, we only focus on

226   the peak-periods that pass the significance test at the 95% confidence level in this study.

227

228   **4 Results**

229   As the first step, we set the embedding dimension m to 11 (within one year) for the SFA and extract the

230   driving-force signals from climate indices, which are denoted as Snino, Ssoi, Spdo, Samo, Snao and Snaoi,

231   respectively. **Fig. 1** shows the variations of these SFA-extracted driving-force signals (red lines) along with

232   the native time series (grey lines) of climate indices. It should be noted that the slowly-varying signals

233   extracted by the SFA are essentially different from the low-frequency signal obtained by low-pass filtering.

234   In contrast to the quickly-varying and lack-of-feature native climate index time series, the slowly-varying

235   signals potentially represent the mixed effects of driving factors.

236

237   **Fig. 2** shows the time-averaged power spectrum of these driving-force signals as reconstructed by SFA. The

238   blue dots indicate the peak-periods that have passed the significant test at the 95% confidence level. Results

239   show that each SFA-extracted signal involves significant peak-periods at inter-annual to multi-decadal

240   timescales. **Table 1** lists the significant peak-periods of each climate indices**.** It is found that four base

241   independent peak-periods (i.e. 2.32 yr, 3.90 yr, 6.55 yr and 11.02 yr) exist among different climate indices.

242   Other peak-periods of the SFA-derived signals from different climate indices can be expressed as integral

243   multiples of above base periods. For the sake of convenience, the above base peak-periods and their

244   corresponding harmonic periods are denoted by integral multiples of T_q (purple), T_{e1} (light blue), T_{e2} (dark

245   blue) and T_s (orange), respectively.

246

247   Furthermore, the peak-period of 2.32 yr (T_q, around 28 months) coincides with the cycle of quasi-biennial

248   oscillation (QBO) (Baldwin et al., 2001), which is the dominant pattern of variability in the tropical

249   stratosphere and displays alternating downward propagating easterly and westerly wind regimes. Although

250   the QBO is a tropical stratospheric phenomenon, it not only affects the chemical constituents (e.g. water

251   vapor, and ozone etc.) but also affects the stratospheric flow from pole to pole by changing the influences of

252   extra tropical waves. Specifically, through the effects on polar vortex, QBO can affect the surface weather

253   patterns indirectly (Baldwin et al., 2001). Previous studies suggested that the temperature gradient between

254   the troposphere and stratosphere can modulate the Walker circulation and SST anomalies in equatorial

255   Pacific Ocean by altering the atmospheric stability and tropical deep convection (Huang et al., 2011).

256

257   We cautiously infer that the two periods (i.e. 3.90 yr (T_{e1}) and 6.55 yr (T_{e2})) are related to the intrinsic

258   inter-annual variability of ENSO activities, and the period of 11.02 yr (T_s) corresponds well to the Schwabe

259   sunspot cycle (11 yr). The results of harmonic analysis shows that the peak-periods of the SFA-derived

260   signals from different climate indices can be expressed as integral multiples of base independent periods (i.e.

261   T_q, T_{e1}, T_{e2} and T_s), implying that these four independent periods associated with QBO, ENSO and solar

262   activity can be regarded as three common driving factors for the variabilities of ENSO, PDO, AMO and

263   NAO.

264

265   Given that the driving-force signal consists of several components, the selection of embedding dimension m

266   might affect the result of phase-space reconstruction of time series (Konen et al., 2009; Yang et al., 2016).

267   Considering that the peak-periods of SFA-extracted driving-force signals may be sensitive to the embedding

268   dimension m as set in SFA, we conduct additional analysis by increasing m from 1 to 25 months (covering

269   two years) to detect the significant peak-periods of these driving-force signals. As **Fig. 3** shows, all the

270   significant peak-periods can be represented as the integral multiples of T_q, T_{e1}, T_{e2} and T_s, which confirms

271   that above-mentioned three driving factors (QBO, the intrinsic variabilities of ENSO, and solar activities)

272   are the common driving factors for the variabilities of ENSO, PDO, AMO and NAO. Note that the

273   significant peak values on a longer time scale are sensitive to the setting of high embedding dimensions,

274   which is probably associated with the smoother SFA signals when setting higher embedding dimensions.

275

276   We further exploit the information involved in **Fig. 3** and decompose them into following tables. **Table 2**

277   shows the number of embedding dimensions by which a peak period is significant for each index. The two

278   columns show periods and the corresponding identifier (forcing), respectively. If this number is greater than

279   10, it is highlighted in bold. Taking Snino for example, the entries in **Table 2** show that 15/25 embedding

280   dimensions have significant peak-value at the period of 74.13 yr ($32T_q$); 12/25 embedding dimensions have

281   significant peak-value at the period of 3.90 yr (T_{e1}); 16/25 embedding dimensions have significant

282   peak-value at the period of 5.51 yr ($0.5T_s$); and 17/25 embedding dimensions have significant peak value at

283   the period of 11.02 yr (T_s).

284   As shown in **Table 2**, each climate mode can be modulated by various driving factors that generate

285   harmonic oscillations at different timescales. For instance, QBO presents four harmonic oscillations from

286   inter-annual (9.27 yr) to multi-decadal (74.13 yr) periods on NINO variability; The intrinsic variability of

287   ENSO presents five harmonic oscillations from intra-seasonal (0.2 yr) to multi-decadal (52.42 yr) timescales

288   on the NAO variability. Similar conditions can be found for other climate indices.

289

290   In addition, it is found that different climate indices involve same driving harmonic oscillations. For instance,

291   both PDO and AMO are modulated by the period of 9.27 yr, which is a QBO-related harmonic oscillation;

292   both NINO and SOI are modulated by the period of 3.90 yr, which we infer is related to intrinsic ENSO

293   cycle; both NINO and PDO are modulated by the inter-annual period of 5.51 yr, which is a harmonic

294   oscillation of solar activity.

295

296   The results displayed in **Fig. 3** and **Table2** can be alternatively presented in **Tables 3** and **4**. In **Table 3**, the

297   columns are the driving force factors (Tq, Te1, Te2 and Ts) and the rows are the climate indices. The entries

298   in the table show the harmonic(s) of driving force factors affecting each index in more than 10 embedding

299   dimensions. It shows that ENSO-Te1 presents the least number of harmonic peak-periods, and that solar,

300   QBO and ENSO-Te2 present equally similar number of peak-periods in shaping the variability of climate

301   indices. Finally, **Table 4** shows the corresponding driving harmonic oscillations that modulate the variability

302   of climate indices in various time scales (periods) for all embedding dimensions. The entries in bold

303   correspond to the gray entries in **Table 2**.

304   In most conditions, as shown in **Table 4**, the driving harmonic oscillations among different climate indices

305   are diverse and complicated in the periods less than 20 yr. Take NAOI for example, there could be up to five

306   driving harmonic oscillations in similar time scales (1-5 yr). Nevertheless, driving harmonic oscillations in

307   the multi-decadal period of 50-55 yr are only related to ENSO –Te2, and the ones in the period of 60-65 yr

308   are only associated with ENSO –Te1. For the driving harmonic oscillations in the period of 70-75 yr, the

309   QBO is identified as the primary influencing factor. The driving harmonic oscillations in the period of 80-85

310   yr are found to be linked to Ts. Above results are useful for improving our understanding of climate

311   variability in different time scales.

312

313   Based on the results obtained by combining SFA with wavelet analysis, we find that all the detected

314   peak-periods can be represented as the integral multiples of the base peak-periods associated with QBO,

315   intrinsic variabilities of ENSO and solar activities. Considering that the time series of AMO used in this

316   study is unsmoothed, we repeat the analysis by using the smoothed AMO index (with a 121-month

317   smoother). The peak-periods detected in the smoothed time series are exactly the same with the ones based

318   on unsmoothed index (figure not shown). This suggests that the pre-processing of the AMO index has little

319   influence on the application results of SFA.

320

321   **5 Conclusions and discussions**

322   In this study, we identify four independent base peak-periods: T_q (2.32 yr), T_{e1} (3.90 yr), T_{e2} (6.55 yr) and T_s

323   (11.02 yr). We infer that these four base peak-periods are essentially associated with the QBO cycle, two

324   intrinsic ENSO cycles and the solar cycle, respectively. Other detected significant peak-periods can be

325   represented by the integral multiples of these four base periods. It implies that the QBO, ENSO and solar

326   activities could be three key periodic driving factors in global climate variability. These results provide

327   possible clues for the intricate relationships between driving forces and their harmonics in the variability of

Earth System
Dynamics
Discussions

328   major climate modes as well as their corresponding coupling ways. The existence of these interconnections

329   of major climate modes indicates that it is promising to develop statistical models to predict the

330   decadal-to-multidecadal climate variability. It should be noted that uncertainties still remain in the

331   multidecadal variability of ENSO and QBO. The relatively long peak-periods (e.g., 52.42 yr, 62.33 yr, 74.13

332   yr and 88.15 yr) detected by SFA may be caused by the influence of the continuous wavelet transform.

333

334   Recent studies on complex climate networks provided new insights into how the collective behavior of

335   major climate modes affects global temperature variations (Tsonis et al., 2007; Tsonis 2018). By considering

336   a network of major climate modes (more or less the same set as here) and the theory of synchronized chaos,

337   these previous studies found that the network may synchronize temporally. During synchronization, the

338   increased coupling strength among the climate modes may lead to the destruction of the synchronized state

339   that leads to changes in the trends of global temperature and the amplitudes of ENSO variability in

340   decadal-to-multidecadal timescales. These studies proposed a dynamical mechanism and its related physical

341   causes for the observed climate shifts. Our results provide further new insights into those physical

342   mechanisms and how the complex interactions among the base driving factors and their harmonics cause the

343   peak-periods in climate modes.

344

345   ***Code/Data availability.*** All data needed to evaluate the conclusions in the paper are present in the paper.

346   Additional data and codes related to this paper may be requested from the corresponding author.

347

348   ***Author contribution.*** Xinnong Pan and Geli Wang designed this study. All of the authors contributed to

349   the preparation and writing of the manuscript.

350

355

356

References

358   Baldwin, M., Gray, L., Dunkerton, T., Hamilton, K., Haynes, P., Randel, W., Horinouchi, T.: The quasi-
359   biennial oscillation. Rev. Geophys., 39, 179-229, 2001.

360   Blaschke, T., Berkes, P., Wiskott, L.: What is the relation between slow feature analysis and independent
361   component analysis? Neural Comput., 18, 2495-2508, 2006.

362   Bjerknes, J.: Atmospheric teleconnections from the equatorial pacific. Mon. Wea. Rev., 97, 163-172, 1969.

363   Bradley, R. S., Diaz, H. F., Kiladis, G. N., Eischeid, J. K.: ENSO signal in continental temperature and
364   precipitation records. Nature, 327, 497-501, 1987.

365   Capotondi, A., Wittenberg, A. T., Newman, M., Di Lorenzo, E., Yu, J. Y., Braconnot, P.: Understanding
366   ENSO diversity. Bull. Amer. Meteor. Soc., 96, 921-938, 2015.

367   Dai, A.: Recent climatology, variability, and trends in global surface humidity. J. Clim., 19, 3589-3606,
368   2006.

369   Dai, A., Fyfe, J. C., Xie, S.-P., Dai, X.: Decadal modulation of global surface temperature by internal
370   climate variability. Nature Clim. Change, 5, 555-559, 2015.

371   Delworth, T. L., Mann, M. E.: Observed and simulated multidecadal variability in the Northern Hemisphere.
372   Clim. Dyn., 16, 661-676, 2000.

373   Delworth, T. L., Zeng, F., Zhang, L., Zhang, R., Vecchi, G. A., Yang, X.: The central role of ocean
374   dynamics in connecting the North Atlantic Oscillation to the extratropical component of the Atlantic
375   Multidecadal Oscillation. J. Clim., 30, 3789-3805, 2017.

376   Deser, C., Alexander, M. A., Xie, S.-P., Phillips, A. S.: Sea surface temperature variability: patterns and
377   mechanisms. Ann. Rev. Mar. Sci., 2, 115-143, 2010.

378   Enfield, D. B., Mestas-Nuñez, A. M., Trimble, P. J.: The Atlantic multidecadal oscillation and its relation to
379   rainfall and river flows in the continental US. Geophys. Res. Lett., 28, 2077-2080, 2001.

380   Escalante-B, A. N., Wiskott, L.: Slow feature analysis: perspectives for technical applications of a versatile
381   learning algorithm. KI-Künstliche Intelligenz, 26, 341-348, 2012.

382   Franzius, M., Wilbert, N., Wiskott, L.: Invariant object recognition with slow feature analysis. Neural
383   Comput., 23, 2289-2323, 2011.

384   Garuba, O. A., Lu, J., Singh, H. A., Liu, F., Rasch, P.: On the relative roles of the atmosphere and ocean in
385   the Atlantic multidecadal variability. Geophys. Res. Lett., 45, 9186-9196, 2018.

386   Huang, B., Hu, Z. Z., Kinter, J. L., Wu, Z., Kumar, A.: Connection of stratospheric QBO with global
387   atmospheric general circulation and tropical SST. part I: methodology and composite life cycle. Clim.
388   Dyn., 38, 1-23, 2012.

389   Hurrell, J., W.: Decadal trends in the North Atlantic Oscillation: regional temperatures and precipitation.
390   Science, 269, 676-679, 1995.

391   Jajcay, N., Hlinka, J., Kravtsov, S., Tsonis, A. A., Paluš, M.: Time-scales of the European surface air
392   temperature variability: The role of the 7-8 year cycle. Geophys. Res. Lett., 43, 902-909, 2016.

393   Jones, P., Jonsson, T., Wheeler, D.: Extension to the North Atlantic Oscillation using early instrumental
394   pressure observations from Gibraltar and South-West Iceland. Int. J. Climatol., 17, 1433-1450, 1997.

395   Kenyon, J., Hegerl, G. C.: Influence of modes of climate variability on global temperature extremes. J. Clim.,
396   21, 3872-3889, 2008.

397   Kirov, B., Georgieva, K.: Long-term variations and interrelations of ENSO, NAO and solar activity. Phys.
398   Chem. Earth, 27, 441-448, 2002.

399   Konen, W., Koch, P.: How slow is slow? SFA detects signals that are slower than the driving force. *arXiv*
400   *preprint arXiv:0911.4397*, 2009.

401   Konen, W., Koch, P.: The slowness principle: SFA can detect different slow components in non-stationary
402   time series. Int. J. Innov. Comp. Appl., 3, 3-10, 2011.

403   Li, J., Sun, C., Jin, F.-F.: NAO implicated as a predictor of Northern Hemisphere mean temperature
404   multidecadal variability. Geophys. Res. Lett., 40, 5497-5502, 2013.

405   Li, J., Wang, X. L. J.: A new NAOI and its variability. Adv. Atmos. Sci., 20, 16, 2003.

406   Liu, Z., Alexander, M.: Atmospheric bridge, oceanic tunnel, and global climatic teleconnections. Rev.
407   Geophys., 45, RG2005, 2007.

408   Mantua, N. J., Hare, S. R., Zhang, Y., Wallace, J. M., Francis, R. C.: A Pacific interdecadal climate
409   oscillation with impacts on salmon production. Bull. Amer. Meteor. Soc., 78, 1069-1079, 1997.

410   Mantua, N. J., Hare, S. R.: The pacific decadal oscillation. J. Ocean., 58, 35-44, 2002.

411   Newman, M., Compo, G. P., Alexander, M. A.: ENSO-forced variability of the Pacific Decadal Oscillation.
412   J. Clim., 16, 3853-3857, 2003.

413   Mccabe, G. J., Palecki, M. A., Betancourt, J. L.: Pacific and Atlantic Ocean influences on multidecadal
414   drought frequency in the United States. PNAS, 101, 4136-4141, 2004.

415   Newman, M., Compo, G. P., Alexander, M. A.: ENSO-forced variability of the Pacific decadal oscillation. J.
416   Clim., 16, 3853-3857, 2003.

417   Newman, M., Alexander, M. A., Ault, T. R., Cobb, K. M., Deser, C., Lorenzo, E. D., Mantua N. J., Miller A.
418   J., Minobe S., Nakamura H., Schneider N., Vimont D. J., Phillips A. S., Scott J. D., Smith C. A.: The
419   pacific decadal oscillation, revisited. J. Clim., 29, 4399-4427, 2016.

420   Pan, X. N., Wang, G. L., Yang, P. C.: Extracting the driving force signal from hierarchy system based on
421   slow feature analysis. Acta Phys. Sin., 66, 080501, 2017.

422   Rayner, N., Parker, D. E., Horton, E., Folland, C., Alexander, L., Rowell, D., Kaplan, A.: Global analyses of
423   sea surface temperature, sea ice, and night marine air temperature since the late nineteenth century. J.
424   Geophys. Res. Atmos., 108, 4407, 2003.

425   Ropelewski, C. F., Jones, P. D.: An extension of the Tahiti–Darwin southern oscillation index. Mon. Wea.
426   Rev., 115, 2161-2165, 1987.

427   Rossi, A., Massei, N., Laignel, B.: A synthesis of the time-scale variability of commonly used climate
428   indices using continuous wavelet transform. Glob. Planet. Change, 78, 1-13, 2011.

429   Schlesinger, M. E., Ramankutty, N.: An oscillation in the global climate system of period 65–70 years.
430   Nature, 367, 723-726, 1994.

431   Steinman, B. A., Mann, M. E., Miller, S. K.: Atlantic and Pacific multidecadal oscillations and Northern
432   Hemisphere temperatures. Science, 347, 988-991, 2015.

433   Sun, C., Li, J., Jin, F.-F.: A delayed oscillator model for the quasi-periodic multidecadal variability of the
434   NAO. Clim. Dyn., 45, 2083-2099, 2015.

435 Torrence, C., Compo, G. P.: A practical guide to wavelet analysis. Bull. Amer. Meteor. Soc., 79, 61-78,

436   1998.

437 Trenberth, K. E., Branstator, G. W., Karoly, D., Kumar, A., Lau, N.-C., Ropelewski, C.: Progress during

438   TOGA in understanding and modeling global teleconnections associated with tropical sea surface

439   temperature. J. Geophys. Res. Atmos., 103, 14291-14324, 1998.

440 Tsonis, A. A.: Insights in climate dynamics from climate networks. Adv. Nonlinear Geosci.: Springer,

441   631-649, 2018.

442 Tsonis, A. A., Swanson, K., Kravtsov, S.: A new dynamical mechanism for major climate shifts. Geophys.

443   Res. Lett, 34, L13705, 2007.

444 Tsonis, A. A., Swanson, K. L., Wang, G.: On the role of atmospheric teleconnections in climate. J. Clim., 21,

445   2990-3001, 2008.

446 Velasco, V., Mendoza, B.: Assessing the relationship between solar activity and some large-scale climatic

447   phenomena. Adv. Space Res., 42, 866-878, 2008.

448 Verdes, P., Granitto, P., Navone, H., Ceccatto, H.: Nonstationary time-series analysis: accurate

449   reconstruction of driving forces. Phy. Rev. Lett., 87, 124101, 2001.

450 Wallace, J. M., Gutzler, D. S.: Teleconnections in the geopotential height field during the northern

451   hemisphere winter. Mon. Wea. Rev., 109, 784-812, 1981.

452 Wang, G. L., Yang, P. C., Zhou, X. J.: Extracting the driving force from ozone data using slow feature

453   analysis. Theor. Appl. Climatol., 124, 985-989, 2016.

454 Wang, G. L., Yang, P. C., Zhou, X. J.: Identification of the driving forces of climate change using the

455   longest instrumental temperature record. Sci. Rep., 7, 46091, 2017.

456 Wang, J., Yang, B., Ljungqvist, F. C., Luterbacher, J., Osborn, T. J., Briffa, K. R., Zorita, E.: Internal and

457   external forcing of multidecadal Atlantic climate variability over the past 1,200 years. Nature Geosci.,

458   10, 512-517, 2017.

459 Wiskott, L.: Estimating driving forces of nonstationary time series with slow feature analysis. *arXiv preprint*

460   *cond-mat/0312317*, 2003.

461 Wiskott, L., Sejnowski, T. J.: Slow feature analysis: Unsupervised learning of invariances. Neural Comput.,

462   14, 715-770, 2002.

463 Wu, R., Hu, Z., Kirtman, B. P.: Evolution of ENSO-related rainfall anomalies in East China. J. Clim., 16,

464   3742-3758, 2003.

465   Xie, T., Li, J., Sun, C., Ding, R., Wang, K., Zhao, C., Feng J.: NAO implicated as a predictor of the surface
466   air temperature multidecadal variability over east Asia. Clim. Dyn., 53, 895–905, 2019.
467   Yang, P. C., Wang, G. L., Zhang, F., Zhou, X. J.: Causality of global warming seen from observations: a
468   scale analysis of driving force of the surface air temperature time series in the Northern Hemisphere.
469   Clim. Dyn., 46, 3197-3204, 2016.
470   Yang, P. C., Bian, J. C., Wang, G. L., Zhou, X. J.: Hierarchy and non-stationarity in climate systems:
471   Exploring the prediction of complex systems. Chin. Sci. Bull., 48, 2148-2154, 2003.
472   Zhang, F., Lei, Y., Yu, Q.-R., Fraedrich, K., Iwabuchi, H.: Causality of the drought in the southwestern
473   United States based on observations. J. Clim., 30, 4891-4896, 2017.
474   Zhang, R.: Anticorrelated multidecadal variations between surface and subsurface tropical north Atlantic.
475   Geophys. Res. Lett., 34, L12713, 2007.
476   Zhang, R.: On the persistence and coherence of subpolar sea surface temperature and salinity anomalies
477   associated with the Atlantic multidecadal variability. Geophys. Res. Lett., 44, 7865–7875, 2017.

478
479
480
481
482
483
484
485
486
487
488
489
490
491
492
493
494
495
496
497
498
499
500
501
502

503

Table 1. The peak-periods of SFA-extracted slow feature signals and their classification.

Snino	3.90	5.51	11.02	74.13			
	T_{e1}	Ts/2	Ts	32Tq			
Ssoi	3.90	6.55	11.02	52.42			
	T_{e1}	Te2	Ts	8Te2			
Spdo	5.51	9.27	18.53	37.06	62.33		
	Ts/2	4Tq	8Tq	16Tq	16Te1		
Samo	9.27	26.21	52.42	74.13			
	4Tq	4Te2	8Te2	32Tq			
Snao	2.75	7.79	11.02	62.33	88.15		
	Ts/4	2Te1	Ts	16Te1	8Ts		
Snaoi	2.75	4.63	7.79	13.10	26.21	44.08	88.15
	Ts/4	2Tq	2Te1	2Te2	4Te2	4Ts	8Ts

504

505

506

507

508

509

510

511

512

513

514

515

516

517

518

https://doi.org/10.5194/esd-2019-74
Preprint. Discussion started: 26 November 2019
© Author(s) 2019. CC BY 4.0 License.

Earth System Dynamics
Discussions
Open Access
EGU

519 **Table 2**. The entries show for each index, the number of embedding dimensions in which a peak period is

520 significant. The left column lists the period and the right column the identifier (forcing). If this number is

521 greater than 10 is highlighted in bold.

Periods	Snino	Ssoi	Spdo	Samo	Snao	Snaoi	identifier
0.58						1	$0.25T_q$
1.16					4		$0.5T_q$
2.32						4	T_q
4.63						7	$2T_q$
9.27	1		**25**	**25**			$4T_q$
18.53	5		**15**		**14**		$8T_q$
37.06	7		**24**				$16T_q$
74.13	**15**	7		**25**			$32T_q$
0.49					2		$T_{e1}/8$
0.97					3	6	$T_{e1}/4$
3.90	**12**	**13**				6	T_{e1}
7.79	7				9	9	$2T_{e1}$
15.58	5					1	$4T_{e1}$
62.33			**25**		**17**		$16T_{e1}$
0.20						1	$T_{e2}/32$
3.28		6			**10**	3	$0.5T_{e2}$
6.55		**20**	6				T_{e2}
13.10	3	**12**	7			3	$2T_{e2}$
26.21		7		**25**		4	$4T_{e2}$
52.42		**17**		**25**		**11**	$8T_{e2}$
2.75					5	4	$0.25T_s$
5.51	**16**		**19**				$0.5T_s$
11.02	**17**	**11**			**20**		T_s
22.04						**12**	$2T_s$
44.08						**10**	$4T_s$
88.15					**15**	**23**	$8T_s$

522

523

524

525

526

527

528

529

530

Earth System Dynamics
Discussions
Open Access
EGU

Table 3. The entries in the table show the harmonics of the basic driving forces (significant when affecting an index in more than 10 different embedding dimensions) for each climate mode index.

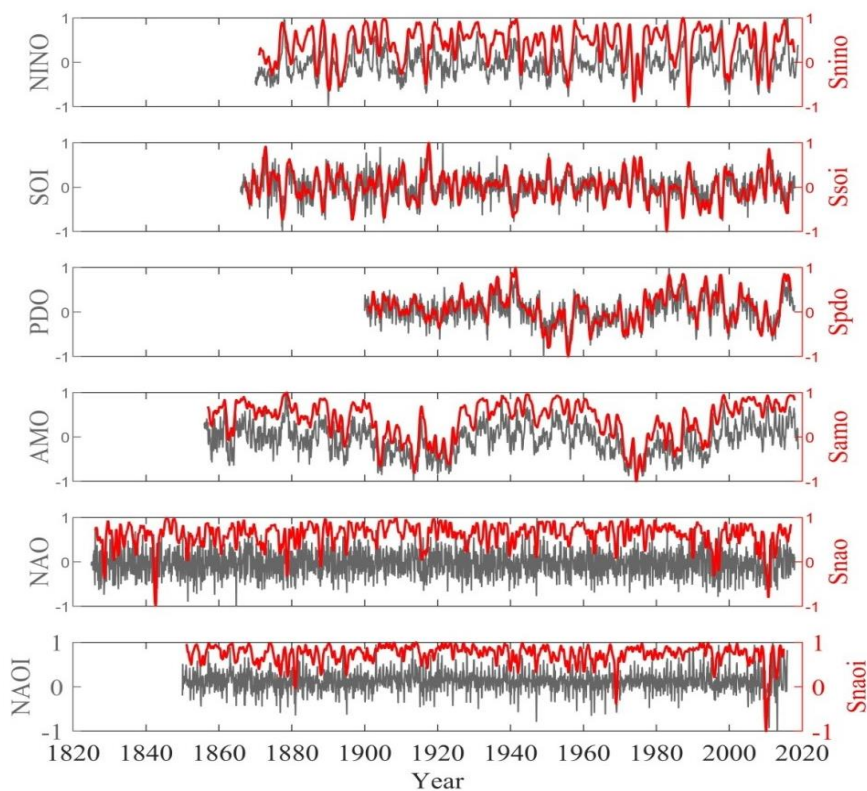| Climate Indices	T_q (QBO)	T_{e1} (ENSO)	T_{e2} (ENSO)	T_s (solar)
Nino	32	1	-	0.5, 1
SOI	-	1	1, 2, 8	1
PDO	4, 8, 16	16	-	0.5
AMO	4, 32	-	4，8	-
NAO	8	16	0.5	1, 8
NAOI	-	-	8	2, 4, 8

Table 4. The basic driving forces and their harmonic oscillations that are associated with the variability of climate mode indices at various time scales (periods) for all embedding dimensions. The entries in bold correspond to the highlighted numbers in **Table 2**.

| Scales	Snino	Ssoi	Spdo	Samo	Snao	Snaoi
<1y					$T_{e1}/8$, $T_{e1}/4$	$0.25T_q$, $T_{e1}/4$, $T_{e2}/32$
1-5y	**T_{e1}**	**T_{e1}**, $0.5T_{e2}$			$0.5T_q$, **$0.5T_{e2}$**, $0.25T_s$	T_q, $2T_q$, T_{e1}, $0.5T_{e2}$, $0.25T_s$
5-10y	$4T_q$, $2T_{e1}$, **$0.5T_s$**	**T_{e2}**	**$4T_q$**, T_{e2}, **$0.5T_s$**	**$4T_q$**	$2T_{e1}$	$2T_{e1}$
10-15y	$2T_{e2}$, **T_s**,	**$2T_{e2}$, T_s**	$2T_{e2}$		**T_s**	$2T_{e2}$
15-20y	$8T_q$, $4T_{e1}$		**$8T_q$**		**$8T_q$**	$4T_{e1}$
20-25y						**$2T_s$**
25-30y		$4T_{e2}$		**$4T_{e2}$**		$4T_{e2}$
30-35y						
35-40y	$16T_q$		**$16T_q$**			
40-45y						**$4T_s$**
45-50y						
50-55y		**$8T_{e2}$**		**$8T_{e2}$**		**$8T_{e2}$**
55-60y						
60-65y			**$16T_{e1}$**		**$16T_{e1}$**	
65-70y						
70-75y	**$32T_q$**	$32T_q$		**$32T_q$**		
75-80y						
80-85y						
85-90y					**$8T_s$**	**$8T_s$**

538

539

540 **Figure 1**. Normalized monthly time series of six climate indices during each periods (gray lines): NINO

541 (01/1870–12/2018), SOI (01/1866–12/2017), PDO (01/1900–12/2017), AMO (01/1856–12/2018), NAO

542 (01/1825–12/2017) and NAOI (01/1850–12/2015); And their corresponding SFA-derived slow feature

543 signals (red lines) , which are indicated by Snino, Ssoi, Spdo, Samo, Snao and Snaoi, respectively (setting

544 embedding dimension m to be 11).

545
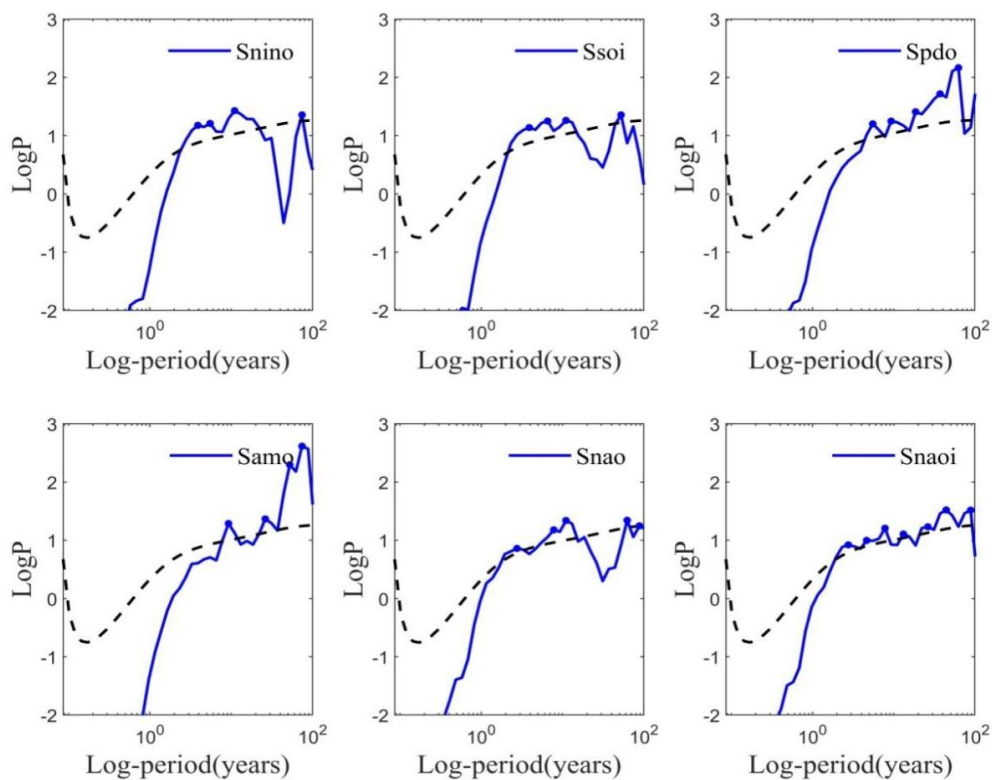
Figure 2. The time-averaged power spectrum of SFA-extracted (m=11) slow feature signals for six climate indices, and the significant points (blue dots) with peak power that pass the significance test at the 95% confidence level (black dashed lines) are also indicated.

549
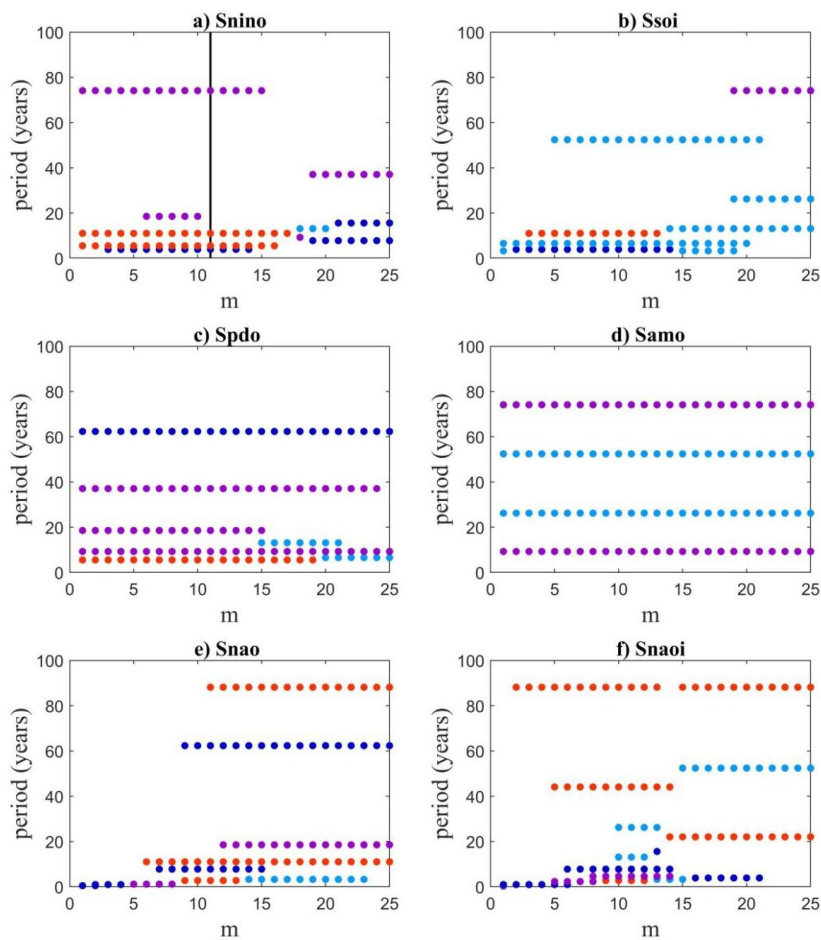
Figure 3. The significant peak periods of the SFA-extracted slow feature signals in six climate indices when

setting different embedding dimensions from 1 to 25.